2008

Scale-dependent desorption of uranium from contaminated subsurface sediments

Chongxuan Liu
Pacific Northwest National Laboratory, chongxuan.liu@pnl.gov

John M. Zachara
Pacific Northwest National Laboratory, john.zachara@pnl.gov

Nikolla P. Qafoku
Pacific Northwest National Laboratory, nik.qafoku@pnl.gov

Zheming Wang
Pacific Northwest National Laboratory, Zheming.wang@pnl.gov

Scale-dependent desorption of uranium from contaminated subsurface sediments

Chongxuan Liu,[1] John M. Zachara,[1] Nikolla P. Qafoku,[1] and Zheming Wang[1]

Received 29 August 2007; revised 1 April 2008; accepted 18 April 2008; published 8 August 2008.

[1] Column experiments were performed to investigate the scale-dependent desorption of uranyl [U(VI)] from a contaminated sediment collected from the Hanford 300 Area at the U.S. Department of Energy (DOE) Hanford Site, Washington. The sediment was a coarse-textured alluvial flood deposit containing significant mass percentage of river cobble. U(VI) was, however, only associated with its minor fine-grained (<2 mm) mass fraction. U(VI) desorption was investigated both from the field-textured sediment using a large column (80 cm length by 15 cm inner diameter) and from its <2 mm U(VI)-associated mass fraction using a small column (10 cm length by 3.4 cm inner diameter). Dynamic advection conditions with intermittent flow and stop-flow events of variable durations were employed to investigate U(VI) desorption kinetics and its scale dependence. A multicomponent kinetic model that integrated a distributed rate of mass transfer with surface complexation reactions successfully described U(VI) release from the fine-grained U(VI)-associated materials. The field-textured sediment in the large column displayed dual-domain tracer-dependent mass transfer properties that affected the breakthrough curves of bromide, pentafluorobenzoic acid (PFBA), and tritium. The tritium breakthrough curve showed stronger nonequilibrium behavior than did PFBA and bromide and required a larger immobile porosity to describe. The dual-domain mass transfer properties were then used to scale the kinetic model of U(VI) desorption developed for the fine-grained materials to describe U(VI) release and reactive transport in the field-textured sediment. Numerical simulations indicated that the kinetic model that was integrated with the dual-domain properties determined from tracer PFBA and Br best described the experimental results. The kinetic model without consideration of the dual-domain properties overpredicted effluent U(VI) concentrations, while the model based on tritium mass transfer underpredicted the rate of U(VI) release. Overall, our results indicated that the kinetics of U(VI) release from the field-textured sediment were different from that of its fine-grained U(VI)-associated mass fraction. However, the desorption kinetics measured on the U(VI)-containing mass fraction could be scaled to describe U(VI) reactive transport in the contaminated field-textured sediment after proper consideration of the physical transport properties of the sediment. The research also demonstrated a modeling approach to integrate geochemical processes into field-scale reactive transport models.

Citation: Liu, C., J. M. Zachara, N. P. Qafoku, and Z. Wang (2008), Scale-dependent desorption of uranium from contaminated subsurface sediments, *Water Resour. Res.*, *44*, W08413, doi:10.1029/2007WR006478.

1. Introduction

[2] Uranium is a common contaminant across the U.S. Department of Energy (DOE) complex, resulting from its use in nuclear fuel for weapons production (Riley and Zachara, 1992). Studies of uranyl[U(VI)]-contaminated sediments from the U.S. DOE Hanford Site have shown that contaminant U(VI) often exists in complex, intragrain or particle coating domains as adsorbed or precipitated uranyl phases [*Arai et al.*, 2007; *Catalano et al.*, 2006; *McKinley et al.*, 2006]. The release of uranium to uncontaminated porewater or groundwater contacting these sediments was typically controlled by kinetic processes that were affected in complex ways by uranyl aqueous and solid speciation, and microscopic physical locations and distribution within the sediment [*Liu et al.*, 2004, 2006; *Qafoku et al.*, 2005]. Such kinetic desorption/dissolution behavior is not unique to contaminated subsurface sediments from Hanford, and has been observed elsewhere [*Braithwaite et al.*, 1997; *Mason et al.*, 1997].

[3] The rate and extent of contaminant U(VI) release has typically been investigated in laboratory systems using reactive mineral fragments or sediment size fraction isolates [e.g., *Curtis et al.*, 2003; *Kohler et al.*, 2004; *Liu et al.*, 2004; *Payne et al.*, 1994, 2001; *Qafoku et al.*, 2005]. Laboratory investigations of this nature provide critical information on

[1]Pacific Northwest National Laboratory, Richland, Washington, USA.

0043-1397/08/2007WR006478

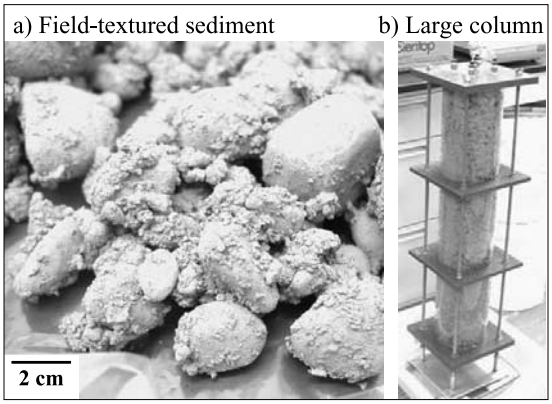

Figure 1. (a) A coarse field-textured sediment from the North Process Pond of U.S. DOE Hanford 300 Area and (b) a large column packed with the field-textured sediment.

the thermodynamics and kinetics of adsorption/desorption and dissolution/precipitation reactions that control the fate and transport of U(VI) in subsurface sediments. The geochemical process models and parameters derived from such studies may be directly applicable to simulate the reactive transport of U(VI) at mesoscopic, or field scales [e.g., *Curtis et al.*, 2006; *Zhu et al.*, 2001]. Often, sorbed U(VI) resides selectively within a specific size, mineral or lithic fragment sub-fraction that may represent a small mass percent of the entire sediment [*Arai et al.*, 2007; *McKinley et al.*, 2006; *Wang et al.*, 2005]. Under these circumstances, process-based geochemical parameters determined by study of reactive mineral or size fractions will require some form of upscaling to describe U(VI) reactive transport in field-textured sediment.

[4] Here we reported an investigation of U(VI) desorption from a field-textured sediment and its fine-grained mass fraction (<2 mm) to which contaminant U(VI) was exclusively sorbed. The objectives of this research are to: (1) evaluate the kinetics of U(VI) desorption from the U(VI)-sorbed mass fraction and its behavior in the field-textured sediment with complex physical transport properties; and (2) develop a numerical approach to upscale U(VI) desorption kinetics to describe U(VI) desorption and reactive transport in large-scale porous media. The sediment was collected from the U.S. DOE Hanford 300 Area where research is underway to investigate subsurface processes controlling U(VI) fate and transport at the field scale. The kinetic release of U(VI) from both coarse, field-textured sediment and its fine-grained (<2 mm), U(VI) -sorbing mass fraction was investigated in column systems under dynamic hydraulic conditions by employing intermittent flow and stop-flow (SF) events with variable SF durations. Laser-induced fluorescence spectroscopy (LIFS) provided insights on the chemical nature of sorbed uranyl species that participated in the adsorption/desorption reactions. The physical transport properties of the subsurface sediment were independently measured or determined using the non-reactive tracers: tritium, Br, and pentafluorobenzoic acid (PFBA). Reactive transport models that integrated the physical transport properties and geochemical processes were used to evaluate the scaling of U(VI) kinetic desorption parameters from the reactive size fraction to the field-textured sediment through comparison of measured and computed advective desorption profiles.

2. Sediment and Characterization

[5] The sediment was collected from the capillary fringe beneath Hanford's historic 300 Area North Process Pond at a depth of about 3 m below ground surface [*Zachara et al.*, 2005]. The sediment was contaminated by U(VI) -containing nuclear fuels fabrication wastes that infiltrated the vadose zone beneath the North Process Pond during the period 1941-1973. A groundwater U(VI) plume exists immediately below the vadose zone with aqueous U(VI) concentrations ranging from 0.3 to 1.1 μmol/L [*Peterson et al.*, 2005]. Groundwater elevation within the plume may vary by a meter or more in response to the stage changes of the nearby Columbia River, resulting in a thick, contaminated capillary fringe zone at the site [*Peterson et al.*, 2005; *Williams et al.*, 2007].

[6] The sediment was a coarse-textured, alluvial flood deposit (Figure 1) that contained a significant mass percentage (75%) of river cobble greater than 12.5 mm in size, 17% smaller cobble or gravel (2.0–12.5 mm), 6% sand (0.053–2 mm), and 2% silt and clay (<0.053 mm) (Table 1). Mineralogical analysis indicated that the sediment was dominated by quartz, feldspars, and hornblende [*Serne et al.*, 2002]. The clay size fraction consisted of muscovite, clinochlore, montmorillonite, and vermiculite, and minor swelling chlorite [*Qafoku et al.*, 2005; *Zachara et al.*, 2005]. Carbonate minerals were a minor component that was detected by chemical extraction [*Zachara et al.*, 2005]. Chemical extractions with citrate-dithionite-carbonate (DCB) and acid ammonium oxalate (AAO) solutions revealed the presence of small amount of non-crystalline and crystalline Fe(III) oxides in the sediment [*Bond et al.*, 2008; *Zachara et al.*, 2005].

[7] The sediment contained 4.0 nmol/g of U(VI) that was detected only in the <2 mm mass fraction (Table 1). The <2mm mass fraction contained 47.8 nmol/g of U(VI) with a much higher concentration (125 nmol/g) in the silt-clay fraction (Table 1). The U(VI) desorption reactions and kinetics in the <2 mm size fraction were quantified to provide insights on the U(VI) behavior in the texturally complex field sediment. Chemical extractions, microscopic and spectroscopic analysis of the solid samples indicated that a significant fraction of sorbed U(VI) was associated with the minor solid phase carbonate minerals in the <2 mm mass fraction [*Zachara et al.*, 2005]. Cryogenic laser-induced florescence spectroscopic (CLIFS) analyses at liquid helium temperature

Table 1. Sediment Size and U(VI) Distributions

	Size Range, mm	Mass Fraction, %	Total U(VI), nmol/g
Cobbles	>12.5	74.5	<22
	2.0–12.5	17.2	<19
Sand	1.0–2.0	2.64	26
	0.5–1.0	2.34	<18
	0.25–0.5	0.78	<21
	0.149–0.25	0.33	37
	0.106–0.149	0.19	<23
	0.053–0.149	0.20	<23
Silt + Clay	<0.053	1.78	125
Sand + Silt + Clay	<2.0	8.30	47.81

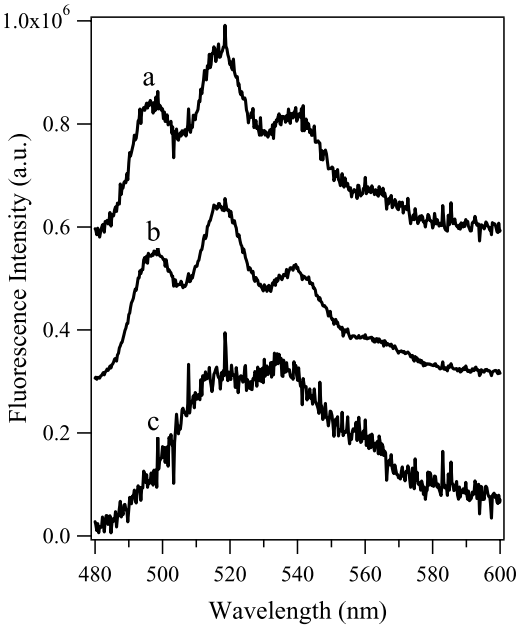

Figure 2. Laser-induced florescence spectroscopic analyses of fine-grained isolates from the sediment showed two distinct U(VI) spectra resembling (spectra a and b) uranyl carbonate and (spectra c) uranyl hydroxide species.

revealed two different florescence components associated with sorbed U(VI) (Figure 2): (1) spectra a and b resembling those for aqueous uranyl carbonate species [*Wang et al.*, 2004], suggesting the presence of uranyl carbonate complexes on mineral surfaces; and (2) spectra c resembling those of uranyl hydroxides [*Wang et al.*, 2008], with peak broadness indicating a surface complex. The CLIFS results (Figure 2) were consistent with the spectroscopic [*Catalano et al.*, 2006; *Arai et al.*, 2007] and chemical extraction results [*Bond et al.*, 2008] that indicated that U(VI) in the sediments from the capillary fringe and groundwater zones existed primarily as adsorbed phases. In contrast, U(VI) in the vadose zone above the capillary fringe existed primarily as dispersed uranyl precipitates as metatorbernite and uranyl carbonate that were embedded in secondary grain-coatings resulting from waste-sediment interactions [*Catalano et al.*, 2006; *Arai et al.*, 2007].

3. U(VI) Desorption Experiments

[8] The desorption of U(VI) from the coarse sediment and its reactive mass fraction (<2 mm) was investigated in column systems using a U(VI) -free, synthetic ground water (SGW) (Table 2) that approximates the composition of natural waters that contact this sediment. The SGW was continuously bubbled with air for at least one week before use to assure equilibrium with atmospheric CO_2(g) and was stored in plastic bottles. Thermodynamic analysis of aqueous speciation and saturation indexes suggested that the SGW was near saturation with respect to calcite, and undersaturated with respect to known U(VI) mineral phases when it contained less than 0.2 μmol/L U(VI), which was the highest U(VI) concentration in the effluent solutions observed in this study. The predominant U(VI) aqueous species were calculated to be $Ca_2UO_2(CO_3)_3$, $CaUO_2(CO_3)_2^{2-}$, $UO_2(CO_3)_2^{2-}$, and $UO_2(CO_3)_3^{4-}$.

[9] The field-textured sediment was packed into a large column (80 cm long x 15 cm inner diameter) to accommodate the large cobbles in the sediment (Figure 1). A total of about 30 kg of the sediment was packed into the large column with a total porosity of 0.32 and bulk density of 1.88 g/cm^3. The sediment was added to the column in a field-moist condition. Column packing was performed in small increments consisting of 2–3 cm thick layers. After each layer addition, the sediment was tamped with a plastic dowel and the exterior wall of the column was gently taped with a plastic hammer to compact the sediment. The sediment mass in the column was determined by tare, and by deducting the moisture content that was determined gravimetrically after drying (80°C). Porous plates (0.25 cm thick and 10 μm pore diameter) were used at the top and bottom of the column to confine the sediment and facilitate the distribution of influent and the collection of effluent solutions.

[10] The column was saturated slowly by injecting the SGW solution from the bottom at a constant flow rate of 1 mL/min. The saturation process took approximately 75 hours. After the saturation, the sediment was leached with the SGW at a constant flow rate of 3.3 mL/min. A high-performance liquid chromatography (HPLC) pump was used to control the flow rate. The intermittent flow and stop-flow (SF) technique with variable SF durations was applied to evaluate mass transfer between aqueous and solid phases and to evaluate whether the U(VI) release from the sediment was equilibrium or kinetically controlled. Effluent samples were collected in an automatic fraction collector. Twelve samples were collected per pore volume during the first 3 days of the experiment and after each SF event; 8 samples per pore volume were collected at other times.

[11] The reactive mass fraction (<2mm size) in the sediment was isolated from the coarse field sediment by dry-sieving. The fine-grained, U(VI) -containing materials were packed in a small column (10.5 cm long and 2.4 cm inner diameter) with a porosity of 0.41 and bulk density of

Table 2. Electrolyte Composition (mmol/L)

	Na	Ca	Mg	K	CO_2(tot)[a]	SO_4	NO_3	SiO_2	pH
Influent	1.53	0.60	0.53	0.43	1.05	0.98	0.57	0.00	8.05
Effluent[b] (small column)	1.25	0.91	0.29	0.10	1.09	0.86	0.54	0.23	7.70
Effluent[c] (large column)	1.79	0.77	0.33	0.21	1.11	0.90	0.58	0.11	7.66

[a]Total dissolved inorganic carbon.
[b]Averaged from small column effluent solution compositions.
[c]Averaged from the large column effluent solution compositions.

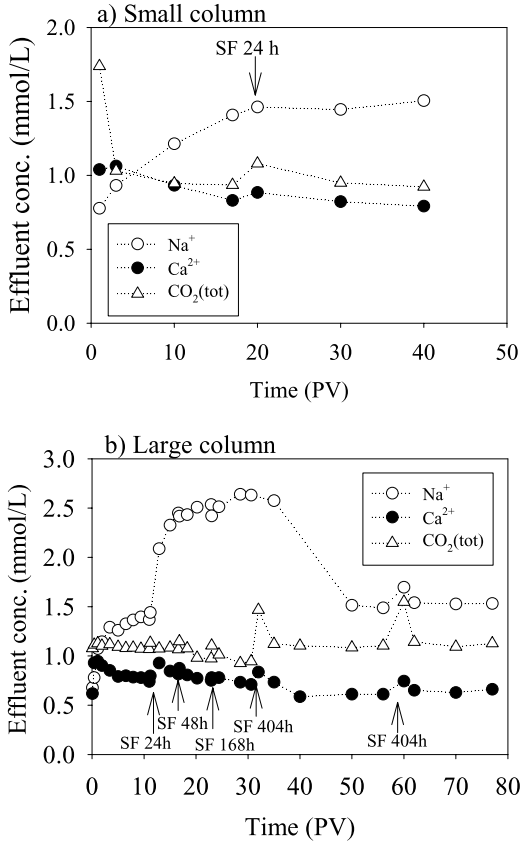

Figure 3. Temporal evolution of aqueous inorganic carbon [CO_2(tot)], Ca^{2+}, and Na^+ concentrations in the effluent solutions during U(VI) desorption from the (a) fine-grained mass fraction in the small column and the (b) field-textured sediment in the large column.

1.56 g/cm^3. The advective desorption experiment in the small column was performed similarly to the large column using the same SGW (Table 2) and the stop-flow advection approach.

[12] The effluent pH from both columns was measured immediately after sample collection. U(VI) in the effluent solutions was analyzed with a kinetic phosphorescence analyzer with a detection limit of 0.001 μmol/L (model KPA-11, Chemchek Instruments, Richland, WA). In select samples, element Ca, Cu, Fe, K, Mg, Mn, Ni, Sr, Na, Si, and S were analyzed with a Perkin Elmer, Optical Emission Spectrometer, Optima 2100DV; total dissolved inorganic carbon was measured with a Dohrman Carbonate analyzer, DC-80; and anion fluoride, chloride, nitrite, nitrate, and phosphate were determined by ion chromatography (IC).

[13] Br was used as a tracer in both the small and large columns to determine the dispersion coefficient and other mass transfer properties. Br was measured using an ion selective electrode (Accumet®). Br transport was measured during and after the U(VI) desorption experiment. Tracer pentafluorobenzoic acid (PFBA) and tritium were also used in the large column to further investigate the mass transfer properties of the coarse porous medium. The PFBA experiment was initiated after the passage of 75 pore volumes of SGW by switching the influent solution to PFBA(20 mg/L) -SGW. The PFBA-spiked SGW had a pH of ~7.85, a value slightly lower than, but close to the pH of the original SGW (pH = 8.05). PFBA was measured by UV/VIS spectroscopy at 262 nm (Shimadzu BioSpec 1601) with a detection limit of 0.1 mg/L, about 200 times lower than its concentration in the influent solution. The tritium experiment was performed after the PFBA experiment by injecting tritium-labeled SGW. The effluent tritium concentration was determined using scintillation counter and associated software (Packard Instrument Co, Meriden, CT). The tritium concentration was measured in total disintegration per minute (DPM), which included the background scintillation count (about 32 DPM) in the influent solution.

4. Numerical Modeling

[14] Numerical models were used in describing tracer transport, U(VI) desorption kinetics, and U(VI) reactive transport in the small and large columns. The models were described in the following individual sections. The goodness of fit of a model to the data was quantified by the root mean square error (RMSE) [*Barnett et al.*, 2002]:

$$\mathrm{RMSE} = \left[\frac{1}{n_d - n_p}\sum_{k=1}^{n_d}\left(\frac{C_k - \hat{C}_k}{C_0}\right)^2\right]^{1/2} \quad (1)$$

where n_d is the number of data points, n_p is the number of adjustable parameters, C_k and $\hat{C}_k$ are the measured and model-calculated concentrations, respectively, and C_0 is the initially measured effluent concentration for desorption cases or the influent concentration for tracer cases. Parameter n_p is zero when a model is used for prediction only.

5. Results and Discussion

5.1. Major Chemical Composition

[15] The solute composition of both the small and large column effluents was dominated by Na^+, K^+, Ca^{2+}, Mg^{2+}, CO_2(tot), NO_3^-, SO_4^{2-}, and H_4SiO_4, among which only silicate solely resulted from SGW-sediment interaction (Table 2). The effluent concentrations of NO_3^- and SO_4^{2-} were constant with time (data not shown) and close to those in the influent solution. The effluent Si concentrations continuously decreased from 0.27 mmol/L at the first pore volume to 0.05 mmol/L at 75th pore volume in the large column, and from 0.30 mmol/L at the first pore volume to 0.15 mmol/L at 125th pore volume in the small column, indicating continued, but decreasing silica dissolution with SGW advective volume. The effluent Ca^{2+} and carbonate concentrations were higher within the first pore volume in the small column and then decreased with increasing time except at SF durations (Figure 3a). In the large column, carbonate concentrations were relatively constant, while Ca^{2+} concentrations continuously decreased with time, except at the SF durations. Effluent concentrations of both Ca^{2+} and carbonate increased immediately after the SF events, and then decreased with time to follow the advective trends. All measured effluent Ca^{2+} concentrations in both the small and large columns were higher than those in the influent solution. The effluent carbonate concentrations were close to the influent concentration in the small column except for the first 3 pore volumes. The decrease in Ca^{2+}

Table 3. U(VI) Aqueous Speciation Reactions Used in the Modeling

Speciation Reaction	log K (I = 0)	Source
$UO_2^{2+} + H_2O = UO_2\ OH^+ + H^+$	−5.25	[a]
$UO_2^{2+} + 2H_2O = UO_2\ (OH)_2(aq) + 2H^+$	−12.15	[a]
$UO_2^{2+} + 3H_2O = UO_2\ (OH)_3^- + 3H^+$	−20.25	[a]
$UO_2^{2+} + 4H_2O = UO_2\ (OH)_4^{2-} + 4H^+$	−32.40	[a]
$2UO_2^{2+} + H_2O = (UO_2)_2\ OH^{3+} + H^+$	−2.70	[a]
$2UO_2^{2+} + 2H_2O = (UO_2)_2\ (OH)_2^{2+} + 2H^+$	−5.62	[a]
$3UO_2^{2+} + 4H_2O = (UO_2)_3\ (OH)_4^{2+} + 4H^+$	−11.90	[a]
$3UO_2^{2+} + 5H_2O = (UO_2)_3\ (OH)_5^+ + 5H^+$	−15.55	[a]
$3UO_2^{2+} + 7H_2O = (UO_2)_3\ (OH)_7^- + 7H^+$	−32.20	[a]
$4UO_2^{2+} + 7H_2O = (UO_2)_3\ (OH)_7^+ + 7H^+$	−21.90	[a]
$UO_2^{2+} + CO_3^{2-} = UO_2CO_3(aq)$	9.94	[a]
$UO_2^{2+} + 2CO_3^{2-} = UO_2(CO_3)_2^{2-}$	16.61	[a]
$UO_2^{2+} + 3CO_3^{2-} = UO_2(CO_3)_3^{4-}$	21.84	[a]
$3UO_2^{2+} + 6CO_3^{2-} = (UO_2)_3(CO_3)_6^{6-}$	54.0	[a]
$2UO_2^{2+} + CO_3^{2-} + 3H_2O = (UO_2)_2CO_3\ (OH)_3^- + 3H^+$	−0.855	[a]
$3UO_2^{2+} + CO_3^{2-} + 3H_2O = (UO_2)_3O(OH)_2HCO_3^+ + 3H^+$	0.655	[a]
$11UO_2^{2+} + 6CO_3^{2-} + 12H_2O = (UO_2)_{11}(CO_3)_6(OH)_{12}^{2-} + 12H^+$	36.43	[a]
$2Ca^{2+} + UO_2^{2+} + 3CO_3^{2-} = Ca_2UO_2(CO_3)_3$	30.70	[b]
$Ca^{2+} + UO_2^{2+} + 3CO_3^{2-} = CaUO_2(CO_3)_3^{2-}$	27.18	[b]
$Mg^{2+} + UO_2^{2+} + 3CO_3^{2-} = MgUO_2(CO_3)_3^{2-}$	26.11	[b]
$UO_2^{2+} + NO_3^- = UO_2NO_3^+$	0.30	[a]

[a] *Guillaumount et al.* [2003].
[b] *Dong and Brooks* [2006].

concentration with time was accompanied by an increase in Na^+ concentration. Effluent Na^+ concentration in the small column increased to that of the influent solution after 20 pore volumes (Figure 3a). In the large column, however, Na^+ concentration increased abruptly from 10 to 35 pore volumes and then decreased toward the influent Na^+ concentration at 50 pore volumes (Figure 3b). The reason for more complex behavior of Na^+ in the large column was unclear. Both K^+ and Mg^{2+} concentrations in the effluent solutions were lower than, but increased with time toward, those in the influent solution (data not shown).

[16] The correlated increase of Na^+ and decrease of Ca^{2+} concentration in the effluent solutions suggested an ion exchange reaction between these solutes and the sediment. Initially, a relatively higher concentration of Na^+ (and K^+ and Mg^{2+} as well) in the influent solution (Table 2) led to the exchange of Na^+ for sorbed Ca^{2+} on the sediment, which led to the higher Ca^{2+} and lower Na^+ concentrations in the effluent solutions. The extent of ion exchange decreased with time as the sediment exchange phase equilibrated with the influent SGW, which led to the increase of Na^+ and decrease of Ca^{2+} concentrations to the influent levels with time. The increase of both effluent Ca^{2+} and carbonate concentrations after the SF events (Figure 3) indicated that the kinetic dissolution of calcium carbonate minerals also contributed to solution composition change. The increase of Na^+ from the SF events may have resulted from the reverse ion exchange reaction of aqueous Ca^{2+} for Na^+ in the sediment, as Ca^{2+} accumulated from carbonate mineral dissolution during the SF durations.

[17] The effluent pH changed only slightly with time (7.63 ± 0.05 for 1–3 PV, 7.71 ± 0.05 for 10–17 PV, 7.75 ± 0.05 for 40–80 PV in the small column; and 7.73 ± 0.04 for 1–10 PV, 7.66 ± 0.04 for 10–20 PV, 7.61 ± 0.08 for 20–30 PV, 7.62 ± 0.05 for 30–60 PV in the large column) and was approximately 0.3 unit lower than that in the influent solution (8.05). Effluent pH also changed slightly before and after the SF events, e.g., pH decreased from 7.72 to 7.58 after 46 hours of SF in the small column, and from 7.61 to 7.51 after 404 hours of SF in the large column. The lower pH in the effluent solutions may have resulted from the pH buffering capacity of the sediment, such as ion exchange reactions of major cations that released H^+. The dissolution of amorphous SiO_2, which provided H_4SiO_4, a major sediment-derived chemical component in the effluent solutions (Table 2), may also have minorly contributed H^+ after partial dissociation of H_4SiO_4 to $H_3SiO_4^-$ and H^+. The dissolution of carbonate minerals would, however, increase pH as CO_3^{2-} accumulated and consumed H^+ to form HCO_3^- under circumneutral pH conditions.

[18] Overall and except for the first 3 PV, the concentrations of Ca^{2+}, CO_2(tot), and pH in the effluent solutions changed only slightly with time (Figure 3). The averaged effluent carbonate concentrations in both the small and large columns were near that in the influent with the Ca^{2+} concentration difference being the largest (Table 2). Aqueous speciation calculations were performed using the chemical compositions in the influent and effluent solutions (Table 2) and using the aqueous U(VI) speciation reactions listed in Table 3. Speciation calculations indicated that the change in aqueous Ca^{2+} concentrations from 0.6 (influent) to 0.9 mmol/L (effluent) had a minimal influence on aqueous U(VI) speciation except for increasing the relative concentration of $Ca_2UO_2(CO_3)_3$(aq) at the expense of $CaUO_2(CO_3)_3^{2-}$. The effects of Mg^{2+} concentration on U(VI) speciation was minor and negligible because of its relatively weak complexation with uranyl (Table 3) and low concentration in the effluent solution (Table 2). The concentrations of Na^+, K^+, and other chemical components had no effect on uranyl speciation.

[19] The averaged concentrations of the major chemical components and pH values in the effluent and influent solutions (Table 2) were used for U(VI) speciation calculations that were required for modeling U(VI) reactive transport in the subsequent analyses. The minor difference in calculated U(VI) speciation using the influent and effluent

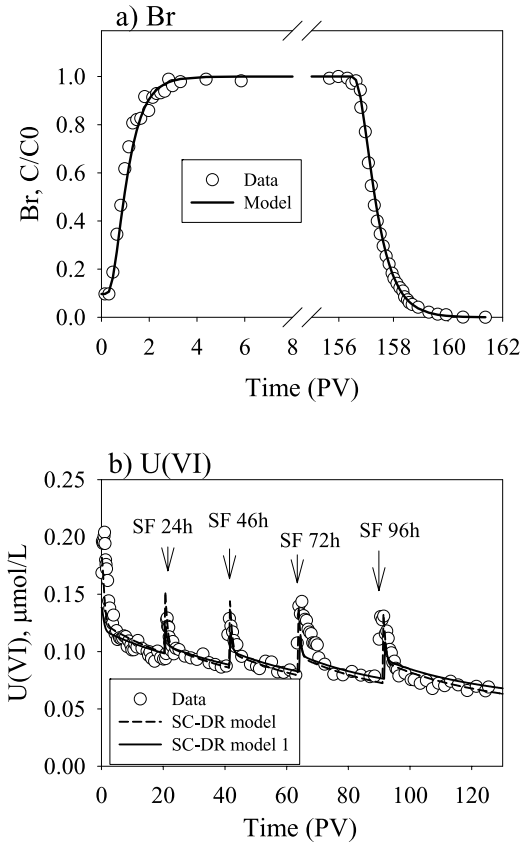

Figure 4. (a) Br breakthrough curve and (b) effluent U(VI) concentrations in the small column. Symbols are the experimental data, and lines are the modeling results. The Br data were modeled with advection and dispersion only. The U(VI) data were modeled with advection and dispersion coupled with U(VI) desorption kinetics that was described by coupling surface complexation reactions with a distributed rate expression (SC-DR) (detail in text). SC-DR model 1 differed from SC-DR model in using equilibrium surface complexation reaction constants (Table 5) and rate constant distribution parameters (Table 4).The RMSE between tracer model and Br data was 0.03, and the RMSE between SC-DR model and data was 0.12, and that between SC-DR model 1 and data was 0.16.

solutions as discussed above justified such simplification. Nevertheless, concentration changes of the chemical components could affect the rate and extent of local U(VI) release along flow path during the initial pore volumes and the SF events when carbonate and Ca^{2+} concentrations deviated from the averaged values.

5.2. U(VI) Desorption Kinetics

[20] The Br breakthrough curve in the small column was symmetric (Figure 4a), and consistent with a model of advection and dispersion using physical parameters in Table 4. The non-zero Br concentration at time zero apparently resulted from the release of Br from the sediment. Br exists in the groundwater of the contaminated field site [*Williams et al.*, 2007]. The porosity (θ), bulk density (ρ_b), and pore velocity (v) (Table 4) were measured values, while the dispersion coefficient was determined by fit to the Br breakthrough curve using the advection and dispersion equation (Figure 4a). The first data point of the measured effluent Br concentration was assumed to be the initial aqueous Br concentration in the column.

[21] The effluent U(VI) concentration was the highest within the first pore volume from the small column, and then quickly decreased to the 5th pore volume with the continuous flush of U-free influent SGW (Figure 4b). After the 5th pore volume, the effluent U(VI) concentration decreased more slowly, suggesting that U(VI) was sorbed to a population of sites with a range in kinetic and/or thermodynamic properties. Moreover, the effluent U(VI) concentration significantly increased immediately after all SF events, indicating that uranyl release was kinetically controlled. Following the spike of the effluent U(VI) concentration after each SF event, there was a period of about 5 pore volumes of quick decrease of effluent U(VI) concentration, followed by a slower one (Figure 4b). This phenomenon was consistent after all the SF events, suggesting that the faster kinetic sites had been recharged by the U(VI) released from the slower kinetic sites during the SF durations.

[22] Beyond the stop-flow spikes, the effluent U(VI) concentrations gradually decreased with time, reflecting the slow depletion of sorbed U(VI) in the sediment. Increasing SF durations at later times only slightly changed the magnitude of the rebounding effluent U(VI) concentration (e.g., 96h in Figure 4b). There was apparently a balance

Table 4. Parameters in Modeling U(VI) Desorption

Parameters	Symbol	Unit	Small Column	Large Column
Column length	L	cm	10.5	80.0
Pore velocity	v	cm/h	8.60	3.52
Dispersion coefficient	D	cm^2/h	15.25	46.52
Total porosity	θ	···	0.41	0.32
Soil bulk density	ρ_b	kg/L	1.56	1.88
Logarithm mean rate	μ	$\log(h^{-1})$	-9.66^a -9.96^b	−9.96
Standard deviation	σ	$\log(h^{-1})$	2.71^a 2.68^b	2.68
Porosity ratio	θ_{im}/θ_m	···	NA	0.20 (PFBA and Br) 0.50 (tritium)
Mass transfer coefficient	ω	h^{-1}	NA	1.45×10^{-2} (PFBA) 3.87×10^{-2} (Br) 4.28×10^{-2} (tritium)

[a]Fitted values when equilibrium constants estimated from the batch data in *Bond et al.* [2008] were used for reactions 2 and 3.
[b]Fitted values when modified equilibrium constants based on the effluent peaks immediately after SF events in Figure 4b were used for reactions 2 and 3 (see text).

between the effect of increasing SF durations which provided more time for the kinetic release of U(VI), and the depletion of U(VI) on the kinetic sites with time, which decreased the thermodynamic driving force for U(VI) desorption.

[23] The multisite, kinetic behavior of U(VI) release from the sediment was consistent with the microscopic and spectroscopic characterizations of the sediment that revealed that sorbed U(VI) existed as adsorbed phases that were associated with mineral surfaces, dispersed in grain coating materials, and/or distributed within intra-aggregates [*Zachara et al.*, 2005]. A distributed rate (DR) model has previously been used to describe such multisite, time-variable mass transfer rates of uranyl adsorption to and desorption from a comparable Hanford 300 Area South Process Pond sediment [*Qafoku et al.*, 2005]. The DR model assumed that the sediment contained a suite of sorption sites that exhibited a range in kinetic properties resulting from either diffusion or chemical kinetic reactions. The mass transfer between the aqueous phase and each sorption site was described by a linear first-order rate expression with a distinct first-order rate constant for each site. To minimize the number of parameters, the first-order rate constants were assumed to follow a statistical distribution, (e.g., gamma distribution defined by two parameters). The mathematical problem of determining a suite of the first-order rate constants was then transferred to a problem of determining the parameters in the statistical distribution. That model, however, used a linear partitioning (K_d) approach to describe U(VI) adsorption and desorption reactions.

[24] A recent investigation found that the equilibrium partitioning of U(VI) between aqueous and solid phases in the Hanford 300 Area sediments could be operationally described using surface complexation reactions of either uranyl carbonate or uranyl hydroxyl species, or their combination [*Bond et al.*, 2008]. Compared with the K_d approach, the surface complexation (SC) model has an advantage that the surface reactions with the same reaction constants could describe the U(VI) equilibrium partitioning under variable solution compositions such as pH and carbonate. In contrast, K_d values have to be varied to describe U(VI) adsorption and desorption under different solution compositions [N. P. Qafoku et al., Evaluation of U(VI) mobility in advancing and retreating zones of a deep vadose zone plume: The role of natural calcite, *Geochimica et Cosmochimica Acta*, 2008]. A surface complexation approach was adopted here to describe U(VI) sorption/desorption reactions. On the basis of the CLIFS spectra (Figure 2) and U(VI) equilibrium partitioning results in a batch system [*Bond et al.*, 2008], the following two U(VI) surface complexation reactions were proposed:

$$> \mathrm{SOH} + \mathrm{UO_2^{2+}} + \mathrm{H_2O} = > \mathrm{SOUO_2OH} + 2\mathrm{H^+} \qquad \mathrm{K_1} \qquad (2)$$

$$> \mathrm{SOH} + \mathrm{UO_2^{2+}} + \mathrm{CO_3^{2-}} = > \mathrm{SOUO_2HCO_3} \qquad \mathrm{K_2} \qquad (3)$$

where >SOH represents a surface site for uranyl adsorption; $>SOUO_2OH$ and $>SOUO_2HCO_3$ are the sorbed uranyl species; other components are aqueous species; and K_1 and K_2 are the equilibrium constants for reactions 2 and 3, respectively. These two reactions have previously been used with reported reaction constants: $\log K_1 = -5.15$ and $\log K_2 = 15.85$, to describe U(VI) sorption and desorption in a set of sediments collected from the capillary fringe and groundwater zones beneath Hanford 300 Area [*Bond et al.*, 2008]. Surface complexation reaction constants are, however, conditioned on aqueous speciation reactions used in modeling and parameter fitting, especially those reactions for dominant aqueous U(VI) species. Under our experimental conditions, species $Ca_2UO_2(CO_3)_3(aq)$ and $CaUO_2(CO_3)_3^{2-}$ are two dominant U(VI) aqueous species. The reaction constants for these two species have recently been updated [*Dong and Brooks*, 2006] with new log K values increased significantly for both species compared with the constants used in *Bond et al.* [2008]. The new reaction constants for these two aqueous species were used in our study (Table 2). Refitting of the batch data in *Bond et al.* [2008] using the reactions and reaction constants listed in Table 2 gave $\log K_1 = -4.29$ and $\log K_2 = 16.66$.

[25] To incorporate the surface complexation reactions (reactions 2 and 3), the DR model described in [*Qafoku et al.*, 2005] was modified to formulate a multicomponent model, as mathematically described by the following equations:

$$\theta\frac{\partial C_i}{\partial t} + (1-\theta)\rho_s\sum_{k=1}^{M}\frac{\partial q_i^k}{\partial t} = \theta D\frac{\partial^2 C_i}{\partial x^2} - \theta v\frac{\partial C_i}{\partial x},\ i = 1,\ 2,\ \ldots,\ N \qquad (4)$$

$$\frac{\partial q_i^k}{\partial t} = \alpha_k\left(S_i^k - q_i^k\right), \quad i = 1,\ 2,\ \ldots, N;\ k = 1,\ 2,\ \ldots, M \qquad (5)$$

where C_i is the total aqueous concentration of chemical component i; q_i^k is the total sorbed concentration of chemical component i at sorption site k; θ is the porosity; ρ_s is the solid density; D is the dispersion coefficient; v is the pore velocity; N is the total number of chemical components in the system; α_k is the rate constant at site k; S_i^k is the adsorption extent of sorbed chemical component i at site k; and M is the total number of sorption sites. Note that equation (5) is similar to the multirate expression commonly used to describe organic contaminant sorption/desorption in subsurface sediments [e.g., *Brusseau et al.*, 1989; *Culver et al.*, 1997; *Haggerty*, 1995; *Villermaux*, 1987]. The difference is that the adsorption extent in the organic multirate expression is expressed by the linear partitioning approach (i.e., $S_i^k = K_d^k C_i$) where the value of S_i^k is only a function of its correspondent aqueous concentration (C_i) and a constant K_d^k at sorption site k. For U(VI), the adsorption extent (S_i^k) has to be calculated from surface complexation reactions (reactions 2 and 3) which are a functions of all related aqueous components (e.g., pH, CO_3^{2-}, U(VI), etc) and sorption site properties (site density and reaction constants). Equation (5) effectively assumes that the kinetic rate of sorption or desorption at site k is proportional to its deviation from the local equilibrium state. The rate constants (α_k, $k = 1, 2, \ldots, M$) in equation (5) were

assumed to follow a lognormal probability distribution to minimize the number of parameters in the model:

$$p(\alpha) = \frac{1}{\sqrt{2\pi}\alpha\sigma} \exp\left(-\frac{1}{2\sigma^2}(\mathrm{In}(\alpha) - \mu)^2\right) \quad (6)$$

where p is the probability of a site that has a correspondent rate constant of α; and μ and σ are the two parameters that define the probability distribution function. Other two-parameter distributions (e.g., gamma distribution) may also be used to describe the rate constants. Our test found that the gamma distribution had no difference from the lognormal distribution in terms of their effectiveness to minimize the number of parameters and describe the rate constant distribution. This was consistent with the literature reports in applying the multirate expression to describe organic sorption/desorption kinetics [e.g., *Culver et al.*, 1997]. Other two-parameter distributions have not been tested, but are expected to work as well. When parameters μ and σ in equation (6) are known, the rate constant α_k in equation (5) can be determined by the following equation.

$$f_k = S_T \int_{\alpha_k - \Delta\alpha/2}^{\alpha_k + \Delta\alpha_k/2} p(\alpha) d\alpha \quad (7)$$

where f_k is defined as the site density for site k that has an averaged rate constant α_k; and S_T is the total sorption site density in the sediment. In the following numerical calculations, f_k for each site was taken as S_T/M. The total uranyl sorption site density (S_T) was estimated to be 7.83×10^{-5} mol/g, which was calculated from a surface area based site density of 3.84 μmol/m^2 [*Bond et al.*, 2008; *Davis and Kent*, 1990] and a measured sediment surface area of 20.4 m^2/g for the fine-grained materials. The same U(VI) sorption site density normalized to surface area was used by *Bond et al.* [2008] to describe U(VI) sorption/desorption reactions in all Hanford 300 Area sediments. With f_k, the adsorption extent of sorbed chemical component i at site k (S_i^k) can be calculated from the surface complexation reactions (Reactions 2 and 3) in equilibrium with local aqueous chemical composition in the column.

[26] Because the concentrations of surface complex species are typically normalized to aqueous volume for mathematical convenience, we define the following new variables:

$$\theta m_i^k = (1-\theta)\rho_s q_i^k \quad (8)$$

$$\theta Q_i^k = (1-\theta)\rho_s S_i^k \quad (9)$$

where m_i^k and Q_i^k are the concentration and adsorption extent of sorbed chemical component i that are normalized to aqueous volume. Replacing equations (8) and (9) into equations (4) and (5) yields:

$$\frac{\partial C_i}{\partial t} + \sum_{k=1}^{M} \frac{\partial m_i^k}{\partial t} = D\frac{\partial^2 C_i}{\partial x^2} - v\frac{\partial C_i}{\partial x}, \quad i = 1, 2, \ldots, N \quad (10)$$

$$\frac{\partial m_i^k}{\partial t} = \alpha_k\left(Q_i^k - m_i^k\right), \qquad i = 1, 2, \ldots, N, \; k = 1, 2, \ldots, M \quad (11)$$

[27] Eight chemical components were considered in calculations, including UO_2^{2+}, CO_3^{2-}, Na^+, Ca^{2+}, Mg^{2+}, NO_3^-, H^+, >SOH; and 43 relevant aqueous species, including those U(VI) species in Table 3, were extracted from our thermodynamic database and used for speciation calculations. All aqueous speciation reactions were treated as equilibrium ones that were used to determine aqueous species concentrations and activities. The Davies expression was used in calculating aqueous activity coefficients. The calculated aqueous species activities were used to calculate the adsorption extent of sorbed chemical components based on surface complexation reactions 2 and 3. As discussed before, the averaged concentrations of the aqueous chemical components (Table 2) were used for the influent and initial aqueous compositions in the column. The total measured U(VI) (T_{UO2}) in the sediment was treated as the initial sorbed uranium concentration, which was assumed to be at equilibrium initially at all sorption sites. The initial concentrations of the two surface complex species at each sorption site were derived from the mass action equations (equations (12) and (13)) that are correspondent to reactions 2 and 3, and a mass balance equation (equation (14)) as follows:

$$[>SOU_2OH] = \frac{K_1[SOH]\{UO_2^{2+}\}}{\{H^+\}^2} \quad (12)$$

$$[>SOU_2HCO_3] = K_2[SOH]\{UO_2^{2+}\}\{CO_3^{2-}\} \quad (13)$$

where bracket { } represents aqueous species activity. Dividing equation (12) by 13 yields:

$$\frac{[>SOUO_2OH]}{[>SOU_2HCO_3]} = \frac{K_1}{K_2\{H^+\}^2\{CO_3^{2-}\}} \quad (14)$$

Assuming that initial aqueous U(VI) in the sediment was negligible, then

$$T_{UO2} = [>SOUO_2OH] + [>SOU_2HCO_3] \quad (15)$$

Equations (14) and (15) defined the initial concentration of each surface complex species. The $\{H^+\}$ and $\{CO_3^{2-}\}$ were determined from the initial aqueous chemical composition.

[28] A sequential iterative scheme was used to numerically solve equations (10) and (11) coupled with the aqueous and surface complexation reactions. Equation (10) was first solved using implicit finite element for the total concentrations of all aqueous chemical components. The total concentrations were used to update the concentrations of aqueous species, which were then used to update the adsorption extent (Q_i^k). The new Q_i^k was used to update the sorbed concentration (m_i^k) of chemical components at each site using equation (11). The updated m_i^k and Q_i^k were used to evaluate adsorption or desorption rates, which were then used to update equation (10) again. This process was

Table 5. Surface Complexation Reactions Used in Modeling

Reactions	log K[a]	log K[b]
$>SOH + UO_2^{2+} + H_2O = >SOUO_2OH + 2H^+$	−4.29	−4.42
$>SOH + UO_2^{2+} + CO_3^{2-} = >SOUO_2HCO_3$	16.66	16.53

[a]Equilibrium constants estimated from the batch data in *Bond et al.* [2008] and used for SC-DR model 1 in Figure 4b.

[b]Modified equilibrium constants based on the effluent peaks immediately after SF events in Figure 4b and used for SC-DR model in Figure 4b and model calculations in Figure 7.

iterated until convergence was achieved for each time step. A global convergence criterion in relative error of 10^{-7} was used.

[29] The SC-DR model, which consists of equations (10) and (11), two mass action equations for the two surface complexation reactions (reactions 2 and 3), and a probability distribution function (equation (6)), contains 6 parameters: two equilibrium constants (K_1 and K_2 for reactions 2 and 3), two kinetic parameters (μ and σ in equation (6)), and two transport parameters (D and v in equation (10)). The values of these parameters used in the numerical simulations that follow are listed in Tables 4 and 5. As described previously, parameter v was experimentally measured and D was determined from the Br breakthrough curve (Figure 4a). The equilibrium constants (log K_1 = −4.29 and log K_2 = 16.66) based on the batch results in *Bond et al.* [2008] were first tried in modeling. Parameters μ and σ in equation (6) were determined to match the U(VI) effluent concentration profile (Figure 4b). Using the equilibrium constants (log K_1 = −4.29 and log K_2 = 16.66), however, the calculated effluent peaks immediately after the SF events were consistently lower than the measured values (solid line in Figure 4b) with fitted μ and σ for equation (6) listed in Table 4. Calculated speciation results (data not shown) during the SF durations indicated that U(VI) desorption was near the equilibrium at the end of each SF event. Consequently, both equilibrium constants were decreased by trial-and-error to match these desorption peaks in the effluent profile. Best match yielded log K_1 = −4.42 and log K_2 = 16.53, which were 0.13 logarithmic unit lower for each constant. The slight deviation of these equilibrium constants were attributed to the measurement errors and variations of sediment properties in Hanford 300 Area capillary fringe and aquifer sediments. The modified equilibrium constants (i.e., log K_1 = −4.42 and log K_2 = 16.53) were used in the subsequent modeling.

[30] The SC-DR model well described the effluent data (short dashed line in Figure 4b) with a RMSE value of 0.12 and fitted parameters μ and σ for equation (6) in Table 4. In the calculation, the first pore volume of the effluent solution was allowed to equilibrate with the sediment in the column to mimic the initial saturation process in the experiment. The higher calculated U(VI) concentration in the initial effluent solution resulted from the kinetic desorption of U(VI) during the column saturation. The measured satura-

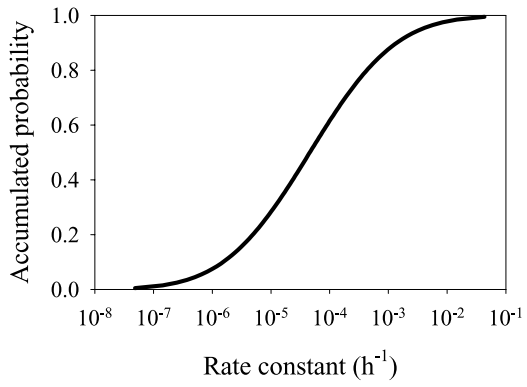

Figure 5. Accumulated probability of the first-order rate constants for the distributed rate model.

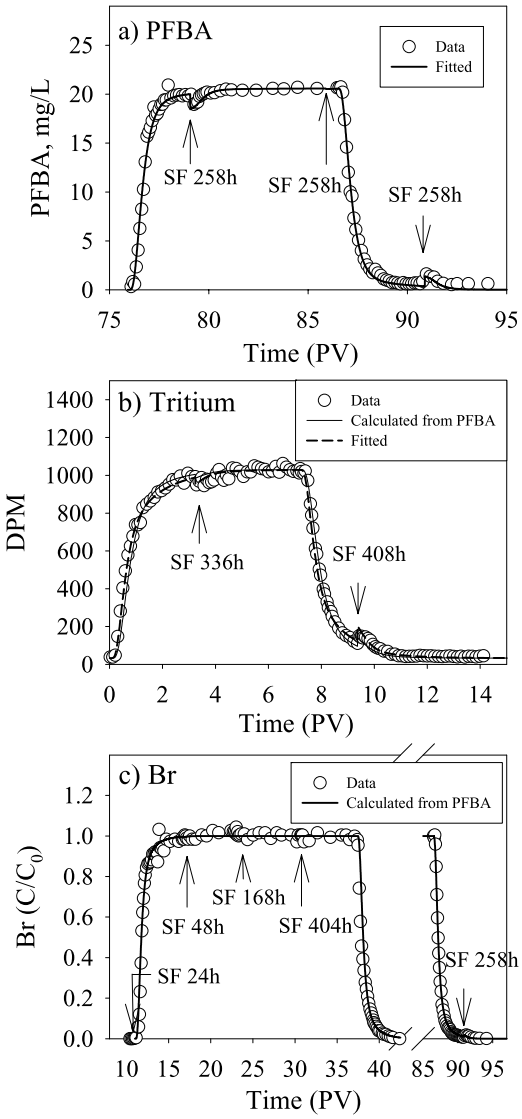

Figure 6. The breakthrough curves of (a) PFBA, (b) tritium, and (c) Br in the field-textured sediment showing nonideal transport behavior. Symbols are the experimental data, and lines are calculated from a dual-domain model (see text). The RMSE for PFBA, tritium, and Br are 0.027, 0.035, and 0.045, respectively, when the pore ratio of immobile to mobile equals 0.2. For tritium, the RMSE improved to 0.025, when the pore ratio of immobile to mobile was increased to 0.5.

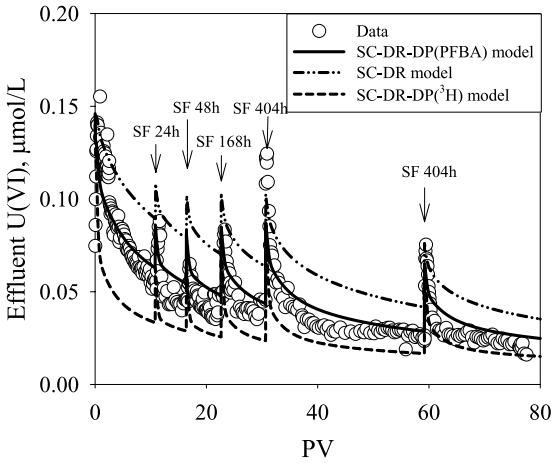

Figure 7. U(VI) desorption from the field-textured sediment in the large column. Symbols are the experimental data, and lines are model-calculated. SC-DR-DP (PFBA or ^{3}H) denotes that U(VI) desorption kinetics were calculated by a model that incorporated the surface complexation (SC) reactions, distributed rate (DR) expression, and dual-domain porosity (DP) with the dual-domain properties determined from tracer PFBA or tritium; SC-DR indicated that U(VI) desorption was calculated by coupling surface complexation (SC) reactions with a distributed rate (DR) expression only (detail in text). The RMSE values for model SC-DR, SC-DR-DP(PFBA), and SC-DR-DP(^{3}H) are 0.39, 0.18, and 0.36, respectively.

tion time (three times of the regular pore residence time) was used in the calculation.

[31] An evaluation of the probability function (equation (6)) using the estimated parameters showed that rate constants ranged from 10^{-7} to 10^{-1} h^{-1} with a cumulative probability >0.1% to <99.9%, respectively (Figure 5), suggesting a wide range of U(VI) sorption sites with different kinetic properties. The reversible rate expression (equation (11)) with a range of kinetic sorption sites (Figure 5) allowed for the fast kinetic sites to be recharged with U(VI) released from the slower kinetic sites during SF durations, explaining the consistent fast decrease of effluent U(VI) concentration followed by slow tailing after each SF event (Figure 4b).

5.3. Tracer Transport in the Field-Textured Sediment

[32] The tracer transports in the large column showed non-ideal behavior (Figure 6). The tritium breakthrough curve was the most asymmetric, followed by PFBA, and then by Br. The greater nonideality of tritium as compared to PFBA and Br likely resulted from charge exclusion effects of fine-grained minerals on anion transports (PFBA and Br) and/or the exchange of tritium for H_2O molecules in clay interlayers [i.e., *Gaber et al.*, 1995; *Hu and Brusseau*, 1996; *Seyfried and Rao*, 1989]. Although the fine-grained materials were less than 2% of the sediment (Table 1), their influence on transport could be disproportionate because of their presence as coatings on large-grains (Figure 1). The SF events (Figure 6) caused a decrease of tracer effluent concentrations on the left edge, and an increase in their concentrations on the right edge of the breakthrough curve, indicating the presence of an immobile mass transfer domain that physically controlled the kinetic behavior in the large column.

[33] The non-ideal breakthrough curves of the tracers were described by a dual-domain mass transfer model:

$$\theta_m \frac{\partial C_m}{\partial t} = \theta_m D \frac{\partial^2 C_m}{\partial x^2} - \theta_m v \frac{\partial C_m}{\partial x} - \omega \theta_{im}(C_m - C_{im}) \quad (16)$$

$$\frac{\partial C_{im}}{\partial t} = \omega(C_m - C_{im}) \quad (17)$$

where C_m and C_{im} are the aqueous concentrations, and θ_m and θ_{im} are the porosities in the mobile and immobile domains, respectively; ω is the mass transfer coefficient between the mobile and immobile regions; and other symbols were as described previously. In the dual-domain model, v and total porosity ($\theta_m + \theta_{im}$) were experimentally measured; the dispersion coefficient (D), the ratio of immobile to mobile porosity (θ_{im}/θ_m), and mass transfer coefficient (ω) were determined by fitting the tracer breakthrough curves using equations (16) and (17). The PFBA breakthrough curve was first used to determine the three parameters in fitting and the determined parameters were then used to describe Br and tritium breakthrough curves after multiplying the mass transfer constant (ω) by a factor of 2.67 and 2.96 for Br and tritium, respectively, to account for their diffusion coefficient differences. Molecular diffusion coefficients at 25°C are 7.78×10^{-10}, 20.8×10^{-10}, and 23.0×10^{-10} m^2/s for PFBA, Br, and ^3H_2O, respectively [*Cussler*, 1995; *Hu and Brusseau*, 1996]. The dual-domain model well described all tracer data of PFBA, tritium, and Br with the parameter values listed in Table 4. The description of the tritium data could be further improved, however, by increasing the ratio of immobile to mobile porosities (Figure 6b, Table 4). The estimated ratio of immobile to mobile porosities was 20% based on PFBA data, which was much smaller than a ratio 50% that best described the tritium data (Table 4). The result was qualitatively consistent with a charge exclusion effect for anion (PFBA and Br) transport and with the tritium diffusion into interlayer regions of clay materials as described before.

5.4. U(VI) Reactive Transport in the Field-Textured Sediment

[34] The effluent profile of uranyl desorption from the field-textured sediment in the large column (Figure 7) was similar to that observed for the < 2mm size fraction in the small column (Figure 4). The effluent U(VI) concentrations from the large column were, however, consistently lower than those in the small column despite a longer flow residence time in the large column (22.7 h) as compared to the small column (1.2 h). These concentration differences in the larger column apparently resulted from the dilution of U(VI) -containing fine-grained materials by large, inert cobbles in the field-textured sediment (Table 1). Numerical simulations using the model described by equations (10) and (11) with: (1) the sorbed U(VI) concentration and sorption sites in the fine-grained materials diluted by the cobbles, and (2) independently determined transport parameters (v, D, and θ), however, overpredicted the effluent

U(VI) concentrations (Figure 7, dashed-dotted line) with a RMSE value of 0.39. The overprediction suggested that the fine-grained materials were also associated with the immobile domain which further decreased the overall rate of U(VI) release from the sediment.

[35] A modification to the previous model was accomplished to incorporate U(VI) desorption kinetics in the reactive sediment fraction with the observed dual-domain properties of the field-textured sediment:

$$\theta_m \frac{\partial C_i^m}{\partial t} + \theta_m \sum_{k=1}^{M} \frac{\partial m_i^{k,m}}{\partial t} = \theta_m D \frac{\partial^2 C_i^m}{\partial x^2} - \theta_m v \frac{\partial C_i^m}{\partial x} - \omega \theta_{im} \left(C_i^m - C_i^{im} \right) \quad (18)$$

$$\frac{\partial m_i^{k,m}}{\partial t} = \alpha_k \left(Q_i^{k,m} - m_i^{k,m} \right) \quad (19)$$

$$\frac{\partial C_i^{im}}{\partial t} + \sum_{k=1}^{M} \frac{\partial m_i^{k,im}}{\partial t} = \omega \left(C_i^m - C_i^{im} \right) \quad (20)$$

$$\frac{\partial m_i^{k,im}}{\partial t} = \alpha_k \left(Q_t^{k,im} - m_i^{k,im} \right) \quad (21)$$

where C_i^m and C_i^{im} are the aqueous concentrations of chemical component i in the mobile and immobile domains, respectively; $m_i^{k,m}$ and $m_i^{k,im}$ are the sorbed concentrations, and $Q_i^{k,m}$ and $Q_i^{k,im}$ are the adsorption extents of sorbed chemical component i at site k, in the mobile and immobile domains, respectively. Both sorbed and adsorption extents were normalized to their respective aqueous pore volumes in the mobile (θ_m) and immobile (θ_{im}) domains. Other parameters were described previously for equations (16) and (17). Equation (18) describes U(VI) advection and dispersion in the mobile domain that was influenced by kinetic adsorption/desorption reactions (equation (19)) in the mobile domain in the sediment; and by the mass exchange between the mobile and immobile domains (equation (20)), which was linked with kinetic adsorption/desorption reactions in the immobile domain (equation (21)). The same SC-DR model that was parameterized for the fine-grain materials was used to describe U(VI) desorption kinetics in the mobile and immobile domains.

[36] The mass transfer coefficient (ω) determined from the PFBA tracer was used to describe the U(VI) mass transfer between the immobile and mobile domains. The diffusion of uranyl in porous media is not well understood because of the potential presence of large number of uranyl species of different size and charge in aqueous solutions [*Guillaumount et al.*, 2003]. One calculation indicated that the diffusion coefficient of $UO_2(CO_3)_3^{4-}$ was 7.2×10^{-10} m^2/s [*Yamaguchi and Nakayama*, 1998], which was close to the PFBA diffusion coefficient in water at 25°C (7.78×10^{-10} m^2/s). The $UO_2(CO_3)_3^{4-}$ complex was a major aqueous species under the experimental conditions.

[37] The total initial U(VI) concentration ($T_{UO2}|_{t=0}$) and sorption site density (T_{SOH}) in the field-textured sediment were computed from the mass percentage of the fine-grained materials in the whole sediment. All U(VI) in the sediment was associated with the fine-grained materials (Table 1) and consequently U(VI) sorption sites in the whole sediment were assumed to only associate with the fine-grained mass fraction. The mass of the fine-grained materials was assumed to be distributed in the mobile and immobile domains according to the ratio of their porosities, i.e. the total initial U(VI) concentration ($T_{UO2}^m|_{t=0}$) and sorption site density (T_{SOH}^m) in the mobile domain were assumed to be $T_{UO2}^m|_{t=0} = T_{UO2}|_{t=0}$ $(1 - \theta_{im}/\theta_m)$ and $T_{SOH}^m = T_{SOH}$ $(1 - \theta_{im}/\theta_m)$, respectively. The total initial U(VI) concentration and sorption site density in the immobile domain were calculated from their differences between the whole sediment and mobile domain.

[38] The initial and influent aqueous concentrations in both immobile and mobile domains were assumed to be the same as the averaged concentrations from the measured influent and effluent solutions in the large column (Table 2). The initial aqueous U(VI) concentrations in both the mobile and immobile domains were assumed to be zero.

[39] A sequential iterative numerical scheme was used in solving equations (18) to (21). Equation (18) was first solved for total aqueous concentrations of all chemical components (C_i^m) in the mobile domain. The total concentrations were then used to update the aqueous species concentrations and activities, and then calculate the adsorption extent ($Q_i^{k,m}$) at each site in the mobile domain. The updated $Q_i^{k,m}$ was then used to solve equation (19) for the sorbed concentrations ($m_i^{k,m}$). The total aqueous concentrations of chemical components in the mobile domain were also used to solve equation (20) for the total aqueous concentrations of chemical components (C_i^{im}) in the immobile domain. The updated C_i^{im} was used to update aqueous speciation and activity in the immobile domain and the adsorption extent ($Q_i^{k,im}$), which was used to solve equation (21) for updated $m_i^{k,im}$. The updated C_i^{im} and $m_i^{k,m}$ were used to calculate the adsorption/desorption kinetic rates in the mobile domain and mass exchange between the mobile and immobile domains, which were used to solve equation (18) again. This process was iterated until convergence with a global convergence criterion of 10^{-7} relative error.

[40] Two simulations were performed using the coupled surface complexation, distributed rate expression, and dual-domain porosity model (SC-DR-DP). The first simulation used the dual-domain properties determined from PFBA that also described Br data (Figure 6), and the other simulation used dual-domain properties from tritium. The simulated effluent U(VI) using the dual-domain properties determined from PFBA matched with the experimental results (RMSE = 0.18), while the model based on the tritium tracer underpredicted the data (RMSE = 0.36) (Figure 7). Both dual domain models, however, improved the simulations compared with that calculated SC-DR model only. The well match between the calculated and measured U(VI) effluent data suggested that U(VI) behaved as anionic PFBA and Br, rather than as neutrally charged tritium, in the dual-domain porous medium. The result was expected because speciation calculations suggested that a significant portion of aqueous U(VI) was presents as anionic uranyl carbonate species that were potentially charge-excluded

from sites that only a neutral, small species, such as tritium, could access through diffusive mass transfer.

6. Conclusions

[41] The fate and transport of uranyl at the field scale is currently under investigation at the Hanford Integrative Field Challenge (IFC) Site at the U.S. DOE Hanford 300 Area. Most contaminated sediments at the site are coarse-textured and contain a significant mass fraction of river cobbles. Uranium is, however, predominately associated with the fine-grained fraction (<2 mm) as adsorbed (as studied here) and/or precipitated phases [e.g., *Arai et al.*, 2007] either on mineral surfaces, or within secondary grain-coating materials, intragrain microfractures, or intra-aggregate domains. Uranyl desorption from the fine-grained materials in an electrolyte representative of Hanford groundwater was controlled by kinetic processes that exhibited multirate behavior. A multicomponent kinetic model that integrated uranyl surface complexation reactions and distributed rate expressions (SC-DR) successfully described the kinetics of U(VI) release from solid to aqueous phases as manifested in the effluent U(VI) concentrations in the column systems. The proposed SC-DR model is flexible in describing U(VI) desorption by linking geochemical reactions through its SC part and kinetics through its DR part. The semi-empirical nature of the SC-DR model that was used in this study, however, requires further evaluation on its applicability under other geochemical conditions.

[42] The apparent rates of U(VI) release from the field-textured sediment was slower than from the fine-grained, U(VI)-associated mass fraction. A model integrating SC-DR kinetics with dual-domain properties was developed to describe the apparent rate of U(VI) release from the field-textured sediment. Model-calculated and experimental results demonstrated that the apparent desorption rates in the field-textured sediment were affected by: (1) dilution of the sorbed U(VI) and sorption site density by inert gravel and river cobble, (2) multiple kinetic rates of U(VI) desorption from solid to aqueous phases, and (3) physical, dual-domain mass transfer properties. The dual-domain mass transfer properties may not be representative of field conditions because a disturbed, homogeneously mixed sediment was used in this study. More complex behavior is likely in the field where the sediments exhibit unique structural attributes from catastrophic flood deposition. However, an important conclusion was that uranyl desorption and reactive transport in the field-textured sediment could be described by integrating: (1) the geochemical reaction network and kinetic parameters derived from laboratory investigations of the reactive mineral or size fraction and (2) physical transport properties of the whole sediment as independently measured by tracer experiments. The modeling approach described in this study provides a means to scale geochemical reaction network and kinetics into reactive transport models for large-scale porous media containing multiple flow domains (dual domains in this case). In this approach, the pore-scale geochemical reactions and multirate kinetics that occurred in the individual flow domains within a finite element were upscaled based on the pore-volumes in the respective flow domains, and the mass exchanges between the individual flow domains were described by the physical mass transfer process that was characterized from tracer experiments. The requirement for this scaling approach for the field-scale application is the field-scale measurements of physical transport properties using tracers, and independent laboratory characterization of geochemical reactions and kinetics.

[43] Different tracers were used to characterize the physical transport properties of the field-textured sediment. A dual-domain model was used to describe the nonideal tracer behavior and was used to upscale the kinetic geochemical reaction network that was quantified for the fine-grained fraction. The assumption that the fine-grained materials were distributed in the dual domains according to their porosity ratio, however, requires further investigation. Based on this approach, our results showed that scaling of the geochemical reactions and kinetics required the use of tracers that had similar mass transport properties as the dominant uranyl species. Ion size, charge, and diffusion rate are among the important considerations in selecting tracers to characterize porous media. For this study, PFBA provided the mass transfer information that best described uranyl reactive transport. Bromide was less effective as a tracer of mobile and immobile domains because of its faster diffusion rate. On the other hand, tritium exhibited enhanced nonideal behavior through contribution of domains that were apparently not accessible to U(VI).

[44] **Acknowledgments.** This research was supported by the U.S. Department of Energy (DOE) through the Environmental Remediation Science Program. The research was also supported by the DOE Environmental Management through the Hanford Remediation and Closure Science Project. Florescence spectroscopic measurements were performed at the Environmental Molecular Sciences Laboratory, a national scientific user facility sponsored by the DOE's Office of Biological and Environmental Research and located at the Pacific Northwest National Laboratory (PNNL). PNNL is operated for the DOE by Battelle Memorial Institute under contract DE-AC06-76RLO 1830. We thank Dr. Yilin Fang at PNNL for providing a geochemical speciation code that was integrated into a multicomponent kinetic model used in this study and Dr. James Davis at U.S. Geological Survey for providing the recalibrated surface complexation reactions and reaction constants for Hanford 300 Area sediment. We also thank Mark Barnett and two anonymous reviewers and Associate Editor Douglas Kent for their constructive comments and suggestions.

References

Arai, Y., M. A. Marcus, N. Tamura, J. A. Davis, and J. M. Zachara (2007), Spectroscopic evidence for uranium bearing precipitates in vadose zone sediments at the Hanford 300-Area site, *Environ. Sci. Technol.*, *41*, 4633–4639.

Barnett, M. O., P. M. Jardine, and S. C. Brooks (2002), U(VI) adsorption to heterogeneous subsurface media: Application of a surface complexation model, *Environ. Sci. Technol.*, *36*, 937–942.

Bond, D. L., J. A. Davis, and J. M. Zachara (2008), Uranium (VI) release from contaminated vadose zone sediments: Estimation of potential contributions from dissolution and desorption, in *Adsorption of Metals by Geomedia II: Variables, Mechanisms, and Model Applications*, edited by M. O. Barnett and D. B. Kent, chap. 14, pp. 375–416, Elsevier, Amsterdam, Netherlands.

Braithwaite, A., F. R. Livens, S. Richardson, and M. T. Howe (1997), Kinetically controlled release of uranium from soils, *Eur. J. Soil Sci.*, *48*, 661–673.

Brusseau, M. L., R. E. Jessup, and P. S. C. Rao (1989), Modeling the transport of solutes influenced by multiprocess nonequilibrium, *Water Resour. Res.*, *25*, 1971–1988.

Catalano, J. G., J. P. McKinley, J. M. Zachara, S. C. Smith, and G. E. J. Brown (2006), Changes in uranium speciation through a depth sequence of contaminated Hanford sediments, *Environ. Sci. Technol.*, *40*, 2517–2524.

Culver, T. B., S. P. Hallisey, D. Sahoo, J. J. Deitsch, and J. A. Smith (1997), Modeling the desorption of organic contaminants from long-term

contaminated soil using distributed mass transfer rates, *Environ. Sci. Technol.*, *31*, 1581–1588.

Curtis, G. P., P. Fox, M. Kohler, and J. A. Davis (2003), Comparison of in situ uranium Kd values with a laboratory determined surface complexation model, *Appl. Geochem.*, *19*, 1643–1653.

Curtis, G. P., J. A. Davis, and D. L. Naftz (2006), Simulation of reactive transport of uranium (VI) in groundwater with variable chemical conditions, *Water Resour. Res.*, *42*, W04404, doi:10.1029/2005WR003979.

Cussler, E. L. (1995), *Diffusion: Mass Transfer in Fluid Systems*, Cambridge Univ. Press, New York.

Davis, J. A., and D. B. Kent (1990), Surface complexation modeling in aqueous geochemistry, in *Mineral-Water Interface Geochemistry, Reviews in Mineralogy*, edited by M. F. Hochella, and A. F. White, pp. 177–260, Mineralogical Society of America, Washington, D. C.

Dong, W., and S. C. Brooks (2006), Determination of the formation constants of ternary complexes of uranyl and carbonate with alkaline earth metal (Mg^{2+}, Ca^{2+}, Sr^{2+}, and Ba^{2+}) using anion exchange method, *Environ. Sci. Technol.*, *40*, 4689–4695.

Gaber, H. M., W. P. Inskeep, S. D. Comfort, and J. M. Wraith (1995), Non-equilibrium transport of atrazine through large intact soil cores, *Soil Sci. Soc. Am. J.*, *59*, 60–67.

Guillaumount, R., T. Fanghänet, V. Neck, J. Fuger, D. A. Palmer, I. Grenthe, and M. H. Rand (2003), *Update on the Chemical Thermodynamics of Uranium, Neptunium, Plutonium, Americium and Technetium*, Elsevier B. V., Amsterdam, Amsterdam, Netherlands.

Haggerty, R. (1995), Aquifer remediation in the presence of rate-limited mass transfer, Stanford Univ., Stanford, Calif.

Hu, Q., and M. L. Brusseau (1996), Transport of rate-limited sorbing solutes in an aggregated porous medium: A multiprocess non-ideality approach, *J. Contam. Hydrol.*, *24*, 53–73.

Kohler, M., D. P. Curtis, D. E. Meece, and J. A. Davis (2004), Methods for estimating adsorbed uranium (VI) and distribution coefficients of contaminated sediments, *Environ. Sci. Technol.*, *38*, 240–247.

Liu, C., J. M. Zachara, O. Qafoku, J. P. McKinley, S. M. Heald, and Z. Wang (2004), Dissolution of uranyl microprecipitates from subsurface sediments at the Hanford Site, USA, *Geochim. Cosmochim. Acta*, *68*, 4519–4537.

Liu, C., J. M. Zachara, W. Yantansee, P. D. Majors, and J. P. McKinley (2006), Microscopic reactive diffusion of uranium in the contaminated sediments at Hanford, USA, *Water Resour. Res.*, *42*, W12420, doi:10.1029/2006WR005031.

Mason, C. F., W. R. Turney, B. M. Thomson, N. Lu, P. A. Longmire, and C. J. Chisholm-Brause (1997), Carbonate leaching of uranium from contaminated soils, *Environ. Sci. Technol.*, *31*, 2707–2711.

McKinley, J. P., J. M. Zachara, C. Liu, and S. M. Heald (2006), Microscale controls on the fate of contaminant uranium in the vadose zone, Hanford Site, Washington, *Geochim. Cosmochim. Acta*, *70*, 1873–1887.

Payne, T. E., J. A. Davis, and T. D. Waite (1994), Uranium retention by weathered schists—the role of iron minerals, *Radiochim. Acta*, *55/56*, 301–307.

Payne, T. E., R. Edis, B. R. Fenton, and T. D. Waite (2001), Comparison of laboratory uranium sorption data with in situ distribution coefficient at the Koongarra uranium deposit, Northern Australia, *J. Environ. Radioact.*, *57*, 35–55.

Peterson, R. E., et al. (2005), *Contaminants of Potential Concern in 300-FF-5 Operable Unit: Expanded Annual Groundwater Report of FY2004*, Pacific Northwest National Laboratory, Richland, Wash.

Qafoku, N. P., J. M. Zachara, C. Liu, P. L. Gassman, O. Qafoku, and S. C. Smith (2005), Kinetic desorption and sorption of U(VI) during reactive transport in a contaminated Hanford sediment, *Environ. Sci. Technol.*, *39*, 3157–3165.

Serne, R. J., C. F. Brown, H. T. Schaef, E. M. Pierce, M. J. Lindberg, Z. Wang, P. L. Gassman, and J. G. Catalano (2002), *300 Area Uranium Leach and Adsorption Project, PNNL-14022*, Pacific Northwest National Laboratory, Richland, Wash.

Seyfried, M. S., and P. S. C. Rao (1989), Solute transport in undisturbed columns of an aggregated tropical soil: Preferential flow effects, *Soil Sci. Soc. Am. J.*, *51*, 1434–1444.

Villermaux, J. (1987), Chemical engineering approach to dynamic modeling of linear chromatography. A simple method for representing complex phenomena from simple concepts, *J. Chromatogr.*, 406.

Wang, Z., J. M. Zachara, W. Yantansee, P. L. Gassman, C. Liu, and A. G. Joly (2004), Cryogenic laser induced fluorescence characterization of U(VI) in Hanford vadose zone pore waters, *Environ. Sci. Technol.*, *38*, 5591–5597.

Wang, Z., J. M. Zachara, J. P. McKinley, and S. C. Smith (2005), Cryogenic laser induced U(VI) fluorescence studies of a U(VI) substituted natural calcite: Implications to U(VI) speciation in contaminated Hanford sediments, *Environ. Sci. Technol.*, *39*, 2651–2659.

Wang, Z., J. M. Zachara, C. Liu, P. L. Gassman, A. R. Felmy, C. Gillespie, and S. B. Clark (2008), A cryogenic flourescence spectroscopic study of uranyl carbonate, phosphate and oxyhydroxide minerals, *Radiochim. Acta*, in press.

Williams, B. A., C. F. Brown, W. Um, M. J. Nimmons, R. E. Peterson, B. N. Bjornstad, D. C. Lanigan, R. J. Serne, F. A. Spane, and M. L. Rockhold (2007), *Limited Field Investigation Report for Uranium Contamination in the 300 Area, 300-FF-5 Operable Unit, Hanford Site, Washington*, Pacific Northwest National Laboratory, Richland, Wash.

Yamaguchi, T., and S. Nakayama (1998), Diffusivity of U, PU, and Am carbonate complexes in a granite from Inada, Ibaraki, Japan studied by through diffusion, *J. Contam. Hydrol.*, *35*, 55–65.

Zachara, J. M., J. A. Davis, C. Liu, J. P. McKinley, N. P. Qafoku, D. M. Wellman, and S. B. Yabusaki (2005), *]Uranium Geochemistry in Vadose Zone and Aquifer Sediments from the 300 Area Uranium Plume, PNNL-15121*, Pacific Northwest National Laboratory, Richland, Wash.

Zhu, C., F. Q. Hu, and D. S. Burden (2001), Multi-component reactive transport modeling of natural attenuation of an acid groundwater plume at a uranium mill tailing site, *J. Contam. Hydrol.*, *52*, 85–108.

C. Liu, N. P. Qafoku, Z. Wang, and J. M. Zachara, Pacific Northwest National Laboratory, PO Box 999, MSIN K8-96, Richland, WA 99352, USA. (chongxuan.liu@pnl.gov)